

# The X-ray Angular Power Spectrum of Extended Sources in the eROSITA Final Equatorial Depth Survey

Erwin T. Lau,<sup>1,2\*</sup> Ákos Bogdán,<sup>1</sup> Urmila Chadayammuri,<sup>1</sup> Daisuke Nagai,<sup>3</sup> Ralph Kraft,<sup>1</sup> and Nico Cappelluti<sup>2</sup>

<sup>1</sup>Center for Astrophysics | Harvard & Smithsonian, 60 Garden St, Cambridge, MA 02138, U.S.A

<sup>2</sup>Department of Physics, University of Miami, Coral Gables, FL 33124, U.S.A.

<sup>3</sup>Department of Physics, Yale University, New Haven, CT 06520, U.S.A.<sup>3</sup>

Accepted XXX. Received YYY; in original form ZZZ

## ABSTRACT

The eROSITA Final Equatorial Depth Survey (eFEDS), with a sky area of 140 square degrees with depth equivalent to the equatorial patch of the final eROSITA all-sky survey, represents the largest continuous non full-sky X-ray fields to-date, making it the premier dataset for measuring the angular power spectrum. In this work, we measure the X-ray angular power spectrum of galaxy clusters and groups in the eFEDS field. We show that the measured power spectrum at large angular scales (multipole  $\ell < 2000$ ) is consistent with that of the ROSAT All Sky Survey, as well as the predictions of cluster gas halo model that is calibrated from Chandra observations of galaxy clusters. At small angular scales ( $\ell > 2000$ ), the eFEDS power spectrum is around an order of magnitude higher than the power spectrum of the Chandra/COSMOS field, and the halo model prediction. A follow-up of the impact of point source contamination with the higher angular resolution instruments like Chandra will resolve this tension. If we restrict the angular scales where eFEDS power agrees with observations and model predictions, we show that the X-ray power spectrum from the upcoming eROSITA all sky data can achieve percent-level constraints on  $\Omega_M$  and  $\sigma_8$ , which are competitive to other cosmological probes.

**Key words:** X-rays: galaxies: clusters – galaxies: clusters: intracluster medium – (cosmology:) large-scale structure of Universe

## 1 INTRODUCTION

Conventional cluster-based cosmological tests rely on counting the number of clusters as a function of redshift (e.g., Vikhlinin et al. 2009; Mantz et al. 2010; Benson et al. 2013). With the advent of large galaxy cluster surveys, the angular clustering of galaxy clusters has emerged as a complementary cosmological probe. This statistics is especially sensitive to the matter density content of the Universe  $\Omega_M$ , and the amplitude of the matter power spectrum,  $\sigma_8$  (Komatsu & Seljak 2002). The galaxy cluster clustering has been measured in the microwave band via the thermal Sunyaev-Zeldovich Effect (tSZ Effect), in which cosmic microwave background (CMB) photons Compton scattered off the hot electron in clusters, resulting in the spectral distortion of the CMB photons. The analysis of the angular power spectrum of the tSZ maps of the *Planck* mission had yielded cosmological constraints that are complimentary to cluster abundance measurements (Planck Collaboration et al. 2016). The cluster power spectrum is also promising in probing neutrino mass (e.g. Bolliet et al. 2020), and models of dark matter, such as sterile neutrinos (Zandanel et al. 2015).

Cluster abundance measurements and power spectra probe cosmology differently and are affected by different systematics. Constraints based on cluster abundances rely on the accurate and precise measurements of galaxy cluster masses and their selection (Pratt et al.

2019). As opposed to this, the angular power spectrum measures the clustering of galaxy clusters and groups over a wide range of masses and redshifts. This, in turn, allows us to probe cluster physics that are otherwise difficult to constrain with individual cluster observations, especially for less massive and high redshift groups that cannot be resolved with current instruments. The X-ray or SZ angular power spectrum can be measured without selection of clusters or deriving their masses by probing the X-ray or SZ clustering signals over a given observed patch of the sky. However, the clustering signal can be contaminated by foreground and background sources. The first measurement of the X-ray angular power spectrum of clusters and groups was performed by Diego et al. (2003), who used the ROSAT all sky survey to place an upper limit on  $\sigma_8$ . Cosmological constraints were also derived by cross-correlating the ROSAT all-sky map with the *Planck* tSZ map (Hurier et al. 2015), subjected to astrophysical uncertainties like non-thermal pressure which changes the amplitude of the tSZ power spectrum (Shaw et al. 2010).

The angular power spectra in X-ray and SZ are sensitive to cluster astrophysics, such as the physics in the outskirts of clusters (Walker et al. 2019), in particular the non-thermal pressure and gas density clumping. These physics are difficult to constrain with individual cluster observations, as the outskirts have low signal-to-noise both in X-ray and SZ given the low gas density and pressure. Angular power spectra, on the other hand, are sensitive to these physics as they measure the total fluctuations of gas properties imposed by these

\* E-mail: erwin.lau@cfa.harvard.edu

physics at scales corresponding to halo outskirts (Shirasaki et al. 2020).

The recently released X-ray data from the eROSITA Final Equatorial-Depth Survey (eFEDS; Brunner et al. 2021) presents a unique dataset to provide the first X-ray power spectrum constraints on both cosmology and astrophysics. Previous X-ray power spectrum measurements with *Chandra* (Kolodzig et al. 2017, 2018) covered only small patches of the sky which lacked the range of angular scales to simultaneously probe both cosmology and cluster astrophysics. The eFEDS field has the largest sky area coverage to date, except the now 30 years old all-sky ROSAT data (Snowden et al. 1997) which has 30 – 50 times lower sensitivity. Before the public release of the eROSITA all sky survey, it remains the best dataset to measure the X-ray power spectrum over a larger range of angular scales. Using eFEDS is also preferable to combining survey data from different X-ray instruments (ROSAT, XMM-Newton, *Chandra*), which have different systematics.

In this paper, we provide the first measurement of the X-ray angular power spectrum of the eFEDS field. We show that the eFEDS X-ray power spectrum is consistent with a model of the X-ray emissions of clusters and groups that is calibrated with independent measurements of density profiles and gas masses of galaxy clusters and groups. While the eFEDS data is still not adequate for providing competitive constraints in cluster astrophysics and cosmology, we show that the constraint will be improved significantly with the all-sky eROSITA data.

The paper is organized as follows. In Section 2, we present and describe the eFEDS data analysis. In Section 3, we describe our model of the X-ray angular power spectrum model. In Section 4, we present our comparison between our model and observations. We provide summary of our results and discussion in Section 5.

Throughout this paper, we assume *Planck*18 cosmology (Planck Collaboration et al. 2020), unless noted otherwise.

## 2 EFEDS DATA ANALYSIS

### 2.1 Construction of the eFEDS Surface Brightness Map

We obtain the raw event files of the eFEDS footprint from the eROSITA-DE Early Data Release website.<sup>1</sup> The eFEDS data consists of four event files, each being a quadrangular patch with an area of 35 square degrees. We use the eSASS software package<sup>2</sup> to perform data reduction and analysis, following Chadayammuri et al. (2022). For each event file, we use the `evt001` command to select all photons with energy between 0.5 – 2.0 keV and convert them into an image count map, with a pixel size of 4 arcsec. We generate the corresponding exposure maps using the `expmap` routine.

Then, we use the CIAO command `reproject_image` to reproject the four images onto the same WCS coordinates, and merge them together into a single field for both the count maps and exposure maps. We exclude detectors T5 and T7 from our analyses, because these were known to have contamination due to defective optical shields (see Chadayammuri et al. 2022 for details).

We divide the counts image by the exposure map to get the count rate map. We then divide the count rate map by the solid angle of the pixels ( $4 \times 4 \text{ arcsec}^2$ ) to get the X-ray surface brightness in  $\text{counts s}^{-1} \text{ sr}^{-1}$ . Figure 1 shows the eFEDS count rate map, which

we use to measure the angular power spectrum. We convert the count rate from  $\text{counts s}^{-1}$  to physical energy units  $\text{erg cm}^{-2} \text{ s}^{-1}$ , using the energy conversion factor of  $1.974 \times 10^{-12} \text{ erg cm}^{-2} \text{ counts}^{-1}$ , assuming an APEC model with 0.4 solar metallicity and a gas temperature of  $10^7 \text{ K}$ .

Resolved point sources are masked out in the X-ray surface brightness map. The point source catalog we used is given in Salvato et al. (2021). Following Chadayammuri et al. (2022), each point source is masked at its position with a circular mask with radius given by the APE-RADIUS parameter in the source catalog, which is the instrumental point spread function (PSF) with size  $\sim 3'$ .

We then interpolate the count rate map in HEALpix pixels (Górski et al. 2005), with  $N_{\text{side}} = 8192$ , with the `reproject` python package. The corresponding angular size of the HEALpix pixel is  $0.25'$  (compared to PSF of  $0.18'$ ). Since eFEDS has a fairly large coverage of  $140 \text{ deg}^2$ , we avoid potential biases of making the flat-sky assumption by using HEALpix projection. The HEALpix interpolated map also allows us to take advantage of the HEALpix analysis package in computing the angular power spectrum.

### 2.2 Excluding Artefacts in eFEDS field

The eFEDS field shown in Figure 1 shows circular features with enhanced surface brightness for declination  $\delta < -0.5^\circ$  that are unnatural. We believe they are artefacts of the instrument or systematics due to scanning strategy. To assess these features from contaminating our power spectrum measurements, we also measure the power spectrum excluding the regions with  $\delta < -0.5^\circ$ .

### 2.3 Measuring the Angular Power Spectrum

The first step to obtain the angular power spectrum is to measure the “pseudo” angular power spectrum, given by

$$\tilde{C}_\ell = \frac{1}{2\ell + 1} \sum_{m=-\ell}^{\ell} a_{\ell m}^* a_{\ell m}, \quad (1)$$

where  $\ell$  is the multipole, which is related to a given angular scale  $\theta$  by  $\ell \sim \pi/\theta$ . Here  $a_{\ell m}$  is the coefficient of the spherical harmonics corresponding to mode  $(\ell, m)$  and  $a_{\ell m}^*$  is its complex conjugate. We use the `anafast` function from `healpy` (Zonca et al. 2019) to compute  $\tilde{C}_\ell$  from multipole  $\ell = 1$  to  $\ell_{\text{max}} = 3N_{\text{side}} - 1 = 24575$ . The relationship between the pseudo angular power spectrum and  $\tilde{C}_\ell$  and the true angular power spectrum  $C_\ell$  is given by

$$\tilde{C}(\ell) = \sum_{\ell'} M(\ell, \ell') C(\ell') B(\ell')^2 + N, \quad (2)$$

where  $B(\ell')$  is the beam transfer function that account for the effect of the point spread function of the instrument,  $M(\ell, \ell')$  is the mode coupling matrix, which describes the coupling of power at different multipoles due to masking and the limited sky coverage, and  $N$  is the power spectrum due to shot noise.

The beam transfer function is  $B(\ell) = \exp(-\ell(\ell + 1)\sigma^2/2)$ , where  $\sigma = \theta_{\text{FWHM}}/\sqrt{8 \ln 2}$  and  $\theta_{\text{FWHM}} = 18 \text{ arcsec}$  is angular PSF of the instrument. We assume the beam to be Gaussian.

The mode coupling matrix  $M(\ell, \ell')$  can be computed analytically (e.g., Hivon et al. 2002) or via Monte-Carlo simulations. We adopt the latter method which is computationally less intensive. We generated 100 mock X-ray surface brightness maps with the same footprint as eFEDS, and their corresponding full sky counterpart using an input model power spectrum based on the ICM model in Section 3. Next, we construct our mock maps using the `synfast` function in

<sup>1</sup> <https://erosita.mpe.mpg.de/edr/eROSITA0bservations/Catalogues/>

<sup>2</sup> <https://erosita.mpe.mpg.de/edr/DataAnalysis/>

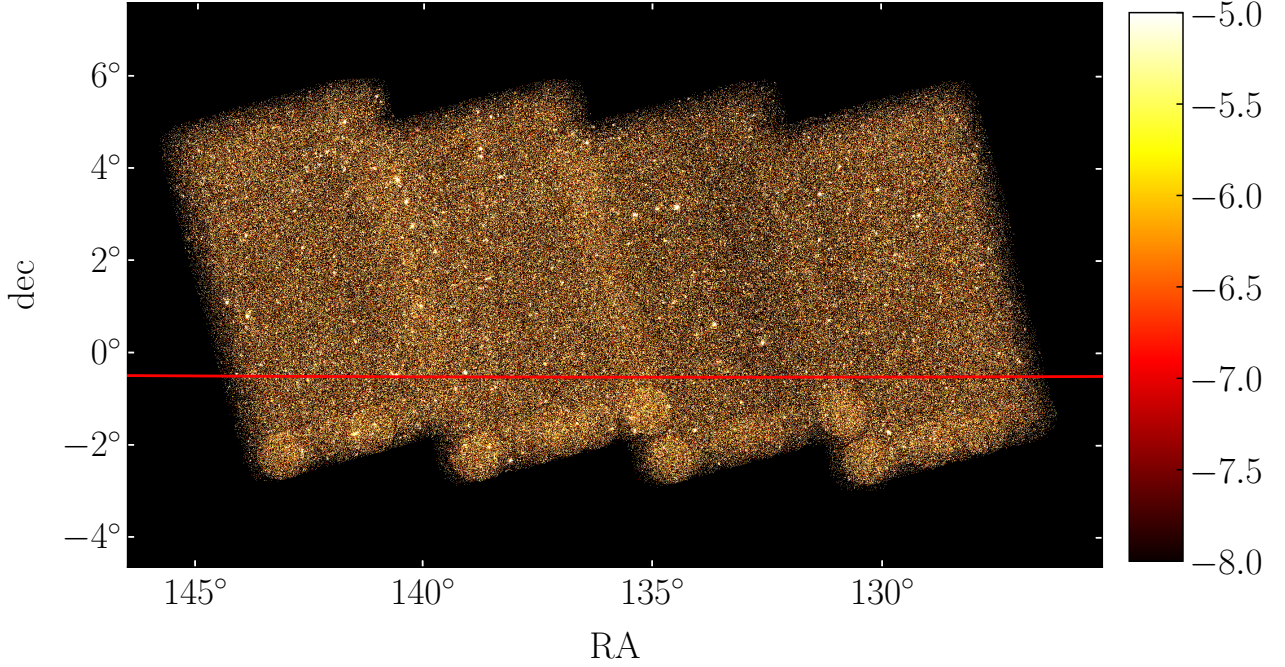


**Figure 1.** The eFEDS photon count rate map (in counts per second) in the [0.5, 2.0] keV band. The scale in the colorbar is in  $\log_{10}$  scale. The red line indicates declination  $\delta = -0.5^\circ$  below where there are visible artefacts. We measured the power spectra with and without this region.

the healpy package. For each map, we measured the power spectra of the eFEDS fields and the full sky map, and we took the average of their differences over the 100 map realizations. The average power spectrum over the mock maps is smaller than the input model power spectrum by the sky fraction  $f_{\text{sky}} = 140 \text{ deg}^2 / (4\pi) = 0.00339$ , where the mock power spectra are smaller than the input by  $f_{\text{sky}}$ . Once we accounted for the sky fraction, we found that there are negligible differences between the power spectra of the eFEDS field and the full-sky field at multipoles greater than 100. The errors on the power spectrum are greater than the difference between the two fields at these multipoles, indicating that mode coupling does not play a significant role at these scales.

While resolved point sources were masked in our eFEDS surface brightness map, the population of unresolved point sources will still contribute. Since these unresolved sources are mainly clustered below the angular resolution and thus contribute to the shot noise power spectrum  $N$ , which needs to be subtracted. As we expect the shot noise to dominate at the smallest angular scales, we determine the total shot noise power spectrum  $N$  by measuring the mean power at the 10 highest  $\ell$  bins (see appendix C in Kolodzig et al. 2017).

We then bin the multipoles in 51 logarithmically spaced bins from  $\ell = 20$  to  $\ell = 20000$ . We estimate the  $1\sigma$  variance of  $C_\ell$  with

$$(\Delta C_\ell)^2 = \frac{2}{2\ell + 1} \frac{(C_\ell + N)^2}{f_{\text{sky}} \Delta \ell}, \quad (3)$$

where  $\Delta \ell$  is the multipole bin width.

## 2.4 Power due to Unresolved Point Sources

We estimate the contribution of power due to clustering of unresolved AGN using the model presented in Helgason et al. (2014) by assuming a step selection function with a flux limit for the eFEDS of  $10^{-14} \text{ erg s}^{-1} \text{ cm}^{-2}$ .

## 3 HALO MODEL POWER SPECTRUM

### 3.1 Modeling the X-ray Auto Power Spectra of Clusters and Groups

We compare the eFEDS X-ray power spectrum with the halo model. In the halo model, the X-ray power at a given angular scale  $\ell$  is given by

$$C_\ell = C_\ell^{\text{1h}} + C_\ell^{\text{2h}}, \quad (4)$$

$$C_\ell^{\text{1h}} = \int_0^{z_{\text{max}}} dz \frac{d^2 V}{dz d\Omega} \times \int_{M_{\text{min}}}^{M_{\text{max}}} dM \frac{dn}{dM} |S_\ell(M, z)|^2, \quad (5)$$

$$C_\ell^{\text{2h}} = \int_0^{z_{\text{max}}} dz \frac{d^2 V}{dz d\Omega} P_{\text{m}}(k_\ell, z) \times \left[ \int_{M_{\text{min}}}^{M_{\text{max}}} dM \frac{dn}{dM} b(M, z) S_\ell(M, z) \right]^2, \quad (6)$$

where  $k_\ell = \ell / \{(1+z)d_A(z)\}$ ,  $z_{\text{max}}$  is the maximum redshift of observed clusters and groups for a given flux-limited X-ray survey,  $d_A(z)$  is the angular diameter distance,  $d^2 V / dz d\Omega = (1 +$



$z)^2 d_A^2 / H(z)$  is the comoving volume per redshift and solid angle. Note that the one-halo term  $C_\ell^{\text{1h}}$  dominates over the two-halo term  $C_\ell^{\text{2h}}$  for the angular scales probed by eFEDS  $\ell > 100$ . We use the Tinker halo mass function  $dn/dM$  and halo mass bias function  $b(M, z)$  (Tinker et al. 2008, 2010) to model the abundance and spatial distributions of dark matter halos, and adopt the flat  $\Lambda$ CDM cosmological parameters from Planck Collaboration et al. (2020), with  $H_0 = 67.3$  km/s/Mpc,  $\Omega_m = 0.315$ ,  $\Omega_b = 0.049$ , and  $\sigma_8 = 0.8159$ , unless noted otherwise. For the same cosmology, we used the linear matter power spectrum  $P(k)$  computed from CAMB<sup>3</sup>, a cosmology code for calculating matter power spectra and transfer functions.

We choose the lower and upper limits of the halo mass to be  $(M_{\min}, M_{\max}) = (10^{13}, 10^{16}) M_\odot$ , covering group and cluster mass scales, and  $z_{\max} = 2.0$  throughout the paper. Almost all of the contribution of the X-ray angular power spectrum comes from halos with mass and redshift within these ranges (see Figure 1 in Shirasaki et al. 2020).

The term  $S_\ell(M, z)$  is the Fourier transform of the X-ray surface brightness profile of halo with mass  $M$  and redshift  $z$  (c.f. Equation 8):

$$S_\ell = \frac{4\pi R_{500}^2}{\ell_{500}^2} \int dx x^2 s_X(x; z) \frac{\sin(\ell x / \ell_{500})}{\ell x / \ell_{500}}, \quad (7)$$

where  $x = r/R_{500}$ ,  $\ell_{500} = d_A/R_{500}$ ,  $R_s$  is the scale radius. The model X-ray emissivity profile  $s_X$  for a given halo is computed as

$$s_X(r; z) = \frac{n_H(r)n_e(r)}{4\pi(1+z)^4} \int_{E_{\min}(1+z)}^{E_{\max}(1+z)} \Lambda(T(r), Z, E) dE, \quad (8)$$

where  $n_H$ ,  $n_e$  and  $T$  are the hydrogen and electron number densities and gas temperature respectively. We use the APEC plasma code version 3.0.9 (Foster et al. 2012) to compute the X-ray cooling function  $\Lambda$ , integrated over energy range at  $z = 0$ :  $[E_{\min}, E_{\max}] = [0.5, 2.0]$  keV in the observer's frame, same as the eFEDS data. We assume constant metallicity of  $Z = 0.3Z_\odot$  throughout the ICM, as suggested from observations (e.g., see Mernier et al. 2018, for review on ICM metallicity).

### 3.2 Halo Gas Model

The profiles of  $n_H$ ,  $n_e$  and  $T$  in Equation 8 are computed with the Baryon Pasting (BP) halo gas model (Osato & Nagai 2022). The halo gas model is described in Shaw et al. (2010) and Flender et al. (2017), which we discussed in more detail in Shirasaki et al. (2020). This model has been used to constrain ICM astrophysics and cosmology with tSZ lensing cross-correlations (Osato et al. 2018, 2020), and mock eROSITA simulations (Comparat et al. 2020). Here we overview the salient features of this model.

The model assumes that the dark matter density profile of the halo follows the Navarro-Frenk-White (NFW) profile (Navarro et al. 1996), which is specified completely by halo redshift, the virial mass of the halo  $M_{\text{vir}}$ , and the halo concentration parameter  $c_{\text{vir}} = R_{\text{vir}}/R_s$  where  $R_{\text{vir}}$  and  $R_s$  are the virial radius and the NFW scale radius, respectively. We use the formulation in Diemer & Kravtsov (2015) to compute the halo concentration for a halo with given mass and redshift.

The total gas pressure (thermal + non-thermal)  $P_{\text{tot}}$  is then assumed to be in hydrostatic equilibrium (HSE) with the gravitational potential of the NFW DM halo in our model. The relationship between the total pressure and the gas density  $\rho_g$  is related

through a polytropic relation, with  $P_{\text{tot}}(r) = P_0 \theta(r)^{n+1}$ , where  $\rho_g(r) = \rho_0 \theta(r)^n$ , and  $\theta(r) = 1 + \frac{\Gamma-1}{\Gamma} \frac{\rho_0}{P_0} (\Phi_0 - \Phi(r))$ . Here  $\theta$  is a dimensionless function that represents gas temperature,  $\Phi_0$  is the central potential of the cluster given by the NFW profile, and  $\Gamma = 1 + 1/n$  is the polytropic exponent, a parameter in our model. Cosmological hydrodynamical simulations suggest that  $\Gamma \approx 1.2$  outside cluster cores where  $r > 0.2R_{500c}$  (Komatsu & Seljak 2002; Ostriker et al. 2005; Shaw et al. 2010; Battaglia et al. 2012). Recent observations show consistent values for this value of the polytropic index (Ghirardini et al. 2019).

The normalization constants  $P_0$  and  $\rho_0$  are then determined numerically by solving the energy and momentum conservation of the ICM. In particular, the energy of the ICM gas is given by

$$E_{g,f} = E_{g,i} + \epsilon_f M_\star c^2 + \Delta E_p. \quad (9)$$

where  $E_{g,f}$  and  $E_{g,i}$  are the final and initial total energies (kinetic plus thermal plus potential) of the ICM.  $\Delta E_p$  is the work done by the ICM as it expands. The term  $\epsilon_f M_\star c^2$  is the energy injected into the ICM due to feedback from both supernovae (SNe) and active galactic nuclei (AGN), where  $M_\star$  is the total stellar mass. Since the X-ray power spectrum is sensitive to the mass of the X-ray emitting gas, rather than the stellar mass in the halo, we modify our model to use the gas mass fraction instead of the stellar mass fraction. The gas mass fraction  $F_{\text{gas}}$  is modeled as

$$F_{\text{gas}}(M_{500}) = f_{\text{gas}} \left( \frac{M_{500}}{3 \times 10^{14} M_\odot} \right)^{S_{\text{gas}}}. \quad (10)$$

which is described by two parameters ( $f_{\text{gas}}, S_{\text{gas}}$ ) that control the normalization and the slope of the  $F_{\text{gas}} - M$  relation. The stellar mass fraction is simply given by subtracting the gas mass fraction from the cosmic baryon fraction  $F_\star = F_{\text{baryon}} - F_{\text{gas}}$ .

Since the X-ray emission from the hot cluster gas is proportional to density squared (as the emission is a two-body process between electron and ion), the X-ray derived gas density will be biased by the gas density clumping factor  $C = \langle n_{\text{gas}}^2 \rangle / \langle n_{\text{gas}} \rangle^2 \geq 1$ . The clumping factor quantifies the level of ‘‘clumpiness’’ in gas density. Cosmological simulations have shown that  $C \gg 1$  in cluster outskirts (Nagai & Lau 2011; Vazza et al. 2013; Zhuravleva et al. 2013). Failing to account for density inhomogeneity will lead to overestimates in gas density and mass (Mathiesen et al. 1999) by the square root of the clumping factor  $\sqrt{C}$ , and also underestimates in hydrostatic mass as it is inversely proportional to gas density (Roncarelli et al. 2013).

Clumping can affect X-ray power spectrum through its gas mass fraction  $F_{\text{gas}}$  dependence. Since with power spectrum alone we will not be able to separately measure the clumping factor, the gas mass fraction we constrain is affected by gas clumping. We therefore merge the clumping dependence into the gas mass fraction parameters  $\sqrt{C} f_{\text{gas}}$ . Here  $C$  represents the gas clumping factor computed within  $R_{500c}$ . Recent observations of nearby clusters place an upper limit on the clumping factor at  $\sqrt{C} \lesssim 1.4$  out to  $R_{200c}$  (e.g. Eckert et al. 2015; Tchernin et al. 2016; Morandi et al. 2017; Mirakhor & Walker 2021).

The model also assumes that the ICM in the dense core of the galaxy cluster follows a different polytropic equation of state than the rest of the ICM due to strong cooling and feedback in the core. Following Flender et al. (2017), we use three parameters to describe the physical state of the ICM in cluster cores:  $x_{\text{break}} = r_{\text{break}}/R_{500}$  where the adiabatic index changes, a separate adiabatic index  $\Gamma_0$  for  $x < x_{\text{break}}$ , and  $\beta_g = d \ln \Gamma_0 / d \ln(1+z)$  models the redshift dependence of  $\Gamma_0$ .

We include the effects of non-thermal pressure in the ICM by adopting the ‘‘universal’’ non-thermal pressure fraction profile from

<sup>3</sup> <https://camb.info>

Parameter	Physical meaning	Fiducial Value
$10^6 \epsilon_f$	feedback efficiency from SNe and AGN	3.97
$\sqrt{C} f_{\text{gas}}$	amplitude of gas mass fraction biased by clumping	0.011
$S_{\text{gas}}$	mass slope of gas mass fraction	0.23
$\Gamma_{\text{mod}0}$	polytropic index within cluster core $r/R_{500c} < 0.2$	0.1024
$A_{\text{nt}}$	amplitude of non-thermal pressure fraction profile	0.451

**Table 1.** Values of the ICM model parameters. They are taken from the best fits of the gas density profiles from *Chandra*-SPT cluster samples from [Flender et al. \(2017\)](#), except the parameters for the non-thermal pressure fraction profile and gas density clumping profile, which are taken from the fit to the *Omega500* cosmological simulation ([Nelson et al. 2014](#)).

[Nelson et al. \(2014\)](#):

$$\frac{P_{\text{nt}}(r)}{P_{\text{th}}(r) + P_{\text{nt}}(r)} = 1 - A_{\text{nt}} \left[ 1 + \exp \left\{ - \left( \frac{r}{B_{\text{nt}} R_{200m}} \right)^{C_{\text{nt}}} \right\} \right]. \quad (11)$$

The model is specified by three parameters  $A_{\text{nt}}$ ,  $B_{\text{nt}}$ , and  $\gamma_{\text{nt}}$ , which represent the normalization, radial dependence, and shape of the non-thermal pressure fraction profile, respectively. These parameters are not well constrained observationally (see [Eckert et al. 2019](#)), thus we take the best fit values from the *Omega500* cosmological simulations ([Nelson et al. 2014](#)) with  $A_{\text{nt}} = 0.451$ ,  $B_{\text{nt}} = 0.841$ , and  $\gamma_{\text{nt}} = 1.628$ . Note that the non-thermal pressure only changes the relative contribution of non-thermal vs thermal pressure in the ICM, thus the X-ray angular power spectrum, which mainly depends on density with weak temperature dependence, is only weakly sensitive to the non-thermal pressure fraction.

### 3.3 Dependence of the X-ray Angular Power Spectrum on Model Parameters

In Figure 2, we show the dependence of the model X-ray angular power spectrum on the key model parameters: the feedback efficiency  $\epsilon_f$ , the normalization  $f_{\star}$  and slope  $S_{\star}$  of the stellar mass fraction, the polytropic exponent in the inner halo core  $\Gamma_{\text{mod},0}$ , the amplitudes of the non-thermal pressure fraction  $A_{\text{nt}}$ , as well as cosmological parameters  $\Omega_M$  and  $\sigma_8$ .

Increasing the feedback efficiency  $\epsilon_f$  decreases gas density inside halo cores, leading to lower X-ray surface brightness (which depends on gas density squared).

Similarly, increasing the gas mass fraction normalization  $\sqrt{C} f_{\text{gas}}$  increases the overall amount of gas mass inside halos, which also leads to higher X-ray emission. Increasing  $S_{\text{gas}}$  increases the amount gas mass in more massive halos with larger angular sizes, thus increases the power spectrum normalization at all scales.

Lowering the polytropic index in the halo core  $\Gamma_{\text{mod},0}$  results in denser halo core gas, which increases X-ray power at small angular scales.

Altering the amplitude of the non-thermal pressure fraction  $A_{\text{nt}}$  also changes the X-ray power spectrum, by changing the temperature of gas in halo. Halos with high non-thermal pressure do not have gas with temperature high enough to be X-ray emitting. Increasing  $\Omega_M$  increases the amount of gas in halos at fixed cosmic baryon fraction, while higher  $\sigma_8$  increases the number of clusters and groups at a given mass and redshift, both leading to increases in the normalization of the X-ray angular power spectrum.

## 4 RESULTS

### 4.1 eFEDS Power Spectrum

Figure 3 shows the resulting X-ray angular power spectrum measured from the eFEDS field with the resolved point sources masked, with both shot noise and unresolved AGN power subtracted. The power spectrum contribution of clustering of unresolved AGN is subdominant at all angular scales. Excluding the region with instrumental artefacts ( $\delta < -0.5^\circ$ ) does not change the measured power spectrum significantly. The artefacts lead to structures at large angular scales ( $\ell_{\text{lesssim}} 100$ ) that are dominated by cosmic variances.

### 4.2 Comparison of eFEDS with Halo Model Power Spectrum

We compare the eFEDS power spectrum with our halo model prediction. The model in general agrees with eFEDS measurements at smaller than  $\ell \sim 2000$ , corresponding to the scale where shot-noise starts to dominate. At larger  $\ell$ , the eFEDS power is larger than the model prediction. The excess is unlikely caused by clustering of unresolved point sources, as the predicted value is small. We believe that the excess could be due to incomplete masking of resolved point sources as we discuss in Section 4.4.

### 4.3 Comparison with Power Spectrum Measurements of ROSAT/SXRB

We compare the power spectrum of eFEDS with that of the Soft X-Ray Background (SXRB) from the ROSAT All Sky Survey ([Snowden et al. 1997](#)). We used the ROSAT/SXRB in HEALpix format (with  $N_{\text{side}} = 512$ ) for analysis<sup>4</sup>. We use the combined R4 and R7 maps for the analysis, which covers the energy range of [0.4, 2.0] keV. We excluded most of the Galactic emissions by masking out regions with galactic latitude between  $l \in [-40^\circ, 40^\circ]$ , and galactic longitude between  $b \in [80^\circ, 250^\circ]$ , with sky fraction  $f_{\text{sky}} = 0.18$ . We follow the same power spectrum estimation procedure described in Section 2.3 for the ROSAT/SXRB measurements. The ROSAT/SXRB power spectrum is limited to  $\ell < 1000$  because of the poor angular resolution of 12 arcmin in SXRB. We find excellent agreement between ROSAT/SXRB and eFEDS at these scales. Note that while the errorbars of the ROSAT/SXRB power spectrum at  $\ell < 200$  are smaller than that of eFEDS, as ROSAT/SXRB has a larger  $f_{\text{sky}} = 0.18$ , compared to 0.034 of eFEDS, the ROSAT/SXRB errorbars are dominated by poisson noise at larger  $\ell$ . It is expected that the full sky eRASS will outperform ROSAT/SXRB with smaller errorbars due to lower poisson noise.

<sup>4</sup> The maps are available at <http://www.jb.man.ac.uk/research/cosmos/rosat/>

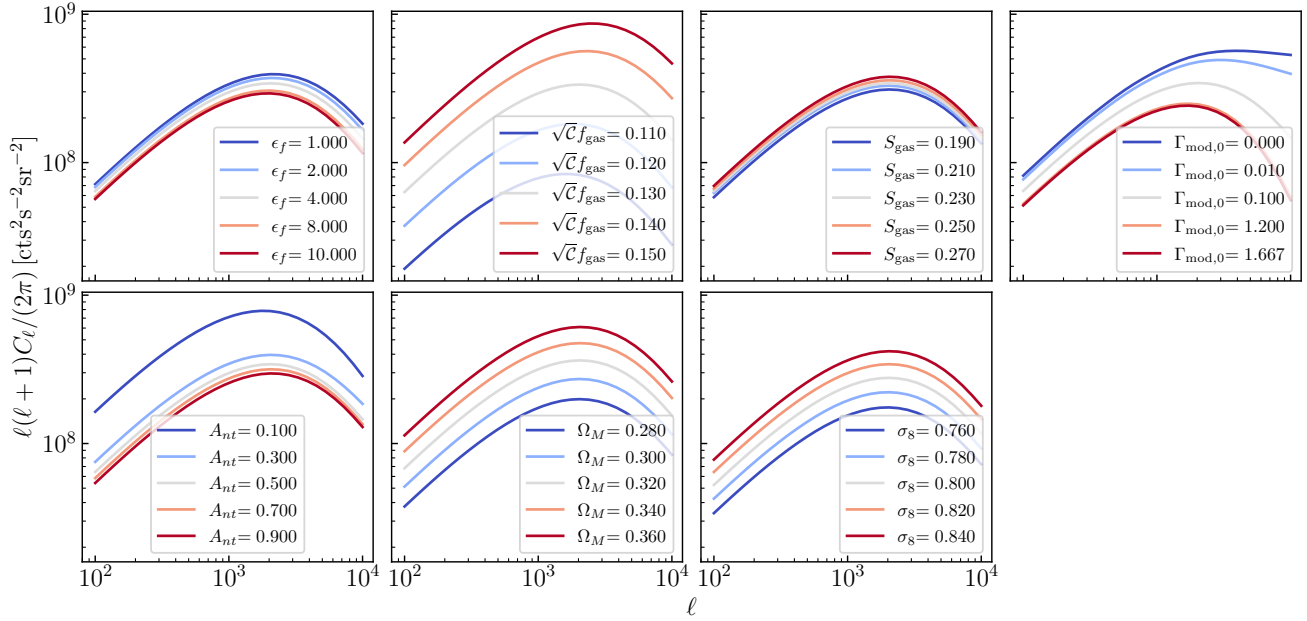


**Figure 2.** Plots showing how the X-ray angular power spectrum depends on the selected parameters of the ICM model listed in Table 1, as well as  $\Omega_M$  and  $\sigma_8$ . In each panel, only one parameter is varied, while the other are fixed to the fiducial values.

#### 4.4 Comparison with Power Spectrum Measurements of Chandra/COSMOS

We also compare the eFEDS power spectrum with the that of the 2.2 deg<sup>2</sup> field of the *Chandra* COSMOS Legacy Survey (Civano et al. 2016). With the high angular resolution of *Chandra* and with relatively deep exposure with an average of 160 ks exposure across the field, the COSMOS field has an extensive catalog of point sources that can be used to evaluate the contribution of unresolved point sources in eFEDS to the power spectrum of extended sources. Following the same power spectrum measurement procedure as in Li et al. (2018), we measure the power spectrum for both resolved and unresolved extended sources in the COSMOS field. Given the limited field of view, we are only able to reliably measure the angular power for multipole  $\ell > 2000$ . When compared with eFEDS, the COSMOS power spectrum has overall lower power at all  $\ell$  range. This suggests that the masking of resolved point sources in the eFEDS field is incomplete, which contaminates the power spectrum measurements of the extended sources. Note that it is unlikely that the excess originates from unresolved point sources, as their clustering power are predicted to be negligible. Thus, the relatively high power at high  $\ell$  is likely due to contamination of the resolved point sources.

#### 4.5 Comparison with Power Spectrum Measurements of Chandra/XBootes

We compare the eFEDS measurements with the X-ray angular power measurements in the *Chandra* XBootes field (Murray et al. 2005). The *Chandra*/XBootes field has an area of 9 deg<sup>2</sup> with an average exposure time of 5 ks. We refer the reader to Kolodzig et al. (2017) and Kolodzig et al. (2018) for details on the power spectrum measurements. The eFEDS power spectrum shows reasonable agreement with that of *Chandra* at  $\ell \in [700, 2000]$ . At  $\ell \lesssim 700$ , corresponding to angular scales of  $\theta > 0.25$  degrees, the power in the *Chandra*/XBootes spectrum underestimates the clustering power, as

it suffers from sample variance due to its relatively small footprint. At higher  $\ell > 2000$ , the error on the *Chandra*/XBootes power becomes too large to make meaningful comparison with eFEDS.

#### 4.6 Cosmological Forecasts for eROSITA All Sky Survey

We perform a Fisher forecast to predict how future all-sky X-ray surveys are able to constrain cluster astrophysics and cosmology. The surveys we consider here are the first (eRASS1) and final (eRASS8) data release of the full-sky scan. The eRASS1 survey will have approximately 1/8th of the exposure than the eRASS8, while eRASS8 will have the same exposure as eFEDS. We consider a sky coverage of 40% for both eRASS1 and eRASS8, for half of the sky that will be made public, and taking into account the masking of the Milky Way Galaxy and other X-ray foregrounds. We compute the Fisher matrix for parameters  $p_i, p_j$  as

$$F_{ij} = \sum_{\ell, \ell'} \frac{\partial C_\ell}{\partial p_i} \Sigma^{-1}(\ell, \ell') \frac{\partial C_{\ell'}}{\partial p_j} \delta_{\ell, \ell'}, \quad (12)$$

where  $\Sigma$  is the covariance matrix in the power spectrum measurements we use the same expression as in Equation 3. For simplicity, we assume that off-diagonal elements are negligible e.g., no mode coupling or mixing of scales in the measurements. This is justified by the low level of correlated errors in the power spectrum measurements at the interested multipole scale  $\ell \in [100, 2000]$  in 30 logarithmic bins. Although we will be able to measure power at higher  $\ell$ , the contamination due to point sources and correlation between point sources and extended sources are uncertain. Thus, we focus in the range of  $\ell \in [100, 2000]$ . The minimal covariance matrix for given two parameters is then the inverse of the Fisher matrix:

$$\text{Cov}(p_i, p_j) = F_{ij}^{-1}. \quad (13)$$

Figure 4 shows our Fisher Forecasts for the astrophysical and cosmological parameters for eRASS1. For eRASS1, even with lower

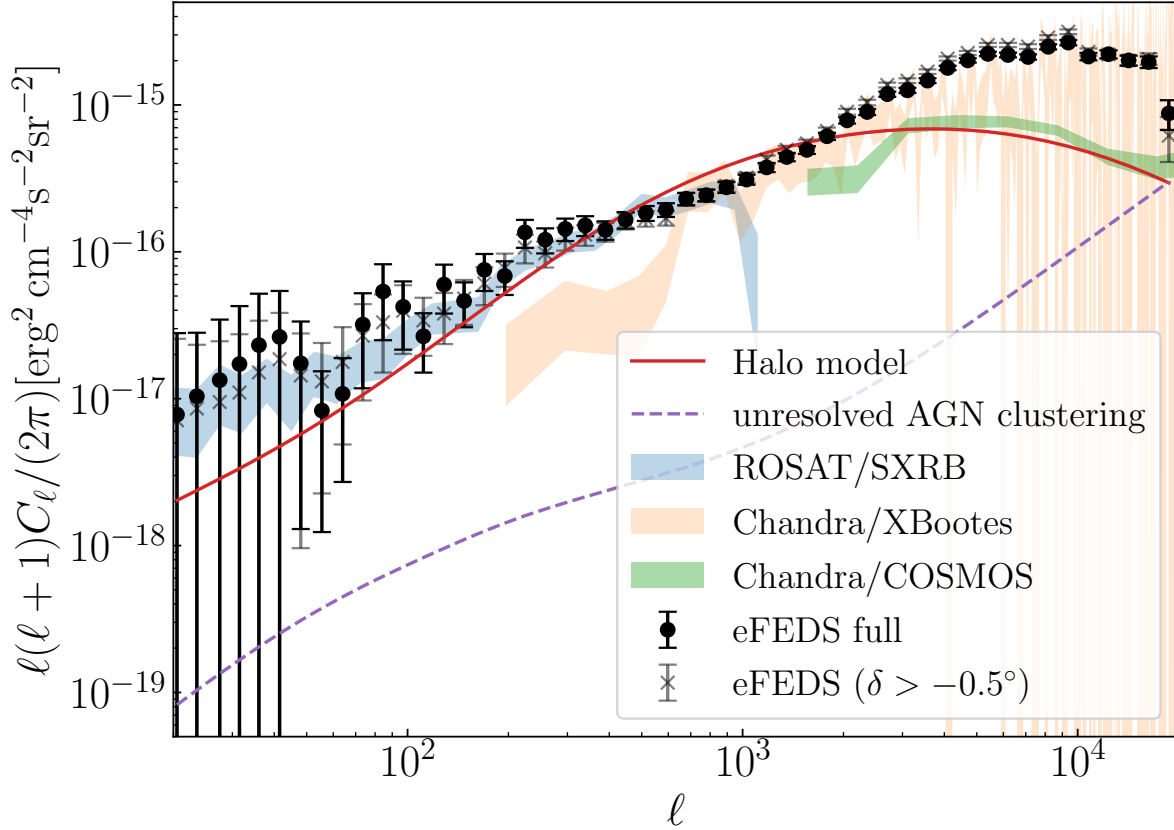


**Figure 3.** The data points represent the X-ray angular power spectra of extended sources measured in the eFEDS field, with and without  $\text{dec} < -0.5^\circ$  excluded (represented by circle and crosses respectively) with  $1\sigma$  errorbars. We also show the  $\pm 1\sigma$  range of the power spectra from three other measurements: ROSAT/SXRB in blue, *Chandra*/XBootes in orange, and *Chandra*/COSMOS in green. The dashed line shows the model power spectrum from clustering of unresolved AGN, and the solid line shows our halo model prediction.

sensitivity than eFEDS, the larger sky coverage can improve the constraints on the parameters. The differences between eRASS1 and eRASS8<sup>5</sup> are minor, as the main uncertainty that limits the power spectrum constraints is sky fraction, which is the same for eRASS1 and eRASS8.

We predict marginalized constraints on  $\Omega_M$  and  $\sigma_8$ , with  $2\sigma$  constraints at 1% and 2% respectively. At the same time, we can achieve  $2\sigma$  constraints on the normalization of the gas mass fraction at 36%, and the normalization of non-thermal pressure fraction at 50%.

Note that these constraints will be improved compared to those obtained in existing cluster counts in X-ray, Microwave, and Optical cluster surveys (Vikhlinin et al. 2009; Mantz et al. 2010; Benson et al. 2013; Mantz et al. 2022), the constraints from cross X-ray and SZ power spectrum measurements with ROSAT-*Planck* (Hurier et al. 2015); and they will be comparable with upcoming cluster count constraints from eRASS (Pillepich et al. 2018).

## 5 SUMMARY AND DISCUSSION

We present the first measurement of the X-ray angular power spectrum of extended sources in the eROSITA Final Equatorial Survey (eFEDS), which covers  $140 \text{ deg}^2$  of the sky. We compare the eFEDS power spectrum measurements to model predictions. Our main findings are the following:

- The power spectrum of extended sources in the eFEDS field is overall consistent with other independent power spectrum measurements at multipoles  $\ell < 2000$ . In particular, it agrees well with the power spectrum of the Soft X-ray Background map from ROSAT All Sky Survey, as well as the smaller *Chandra*/XBootes and COSMOS fields.
- At  $\ell > 2000$ , the eFEDS power spectrum shows more power than the power spectra of the *Chandra* XBootes and COSMOS fields by an order of magnitude.
- The model X-ray power spectrum, based on calibration from a *Chandra* measurements of density profiles of the South-Pole Telescope cluster sample, provides a reasonably good match to the eFEDS power spectrum at multipoles  $\ell < 2000$  without any fitting or fine-tuning of the parameters. However, for  $\ell > 2000$ , the eFEDS power is higher than the model power spectrum by an order of magnitude.

<sup>5</sup> At this point, it is not clear whether eRASS8 will be completed.

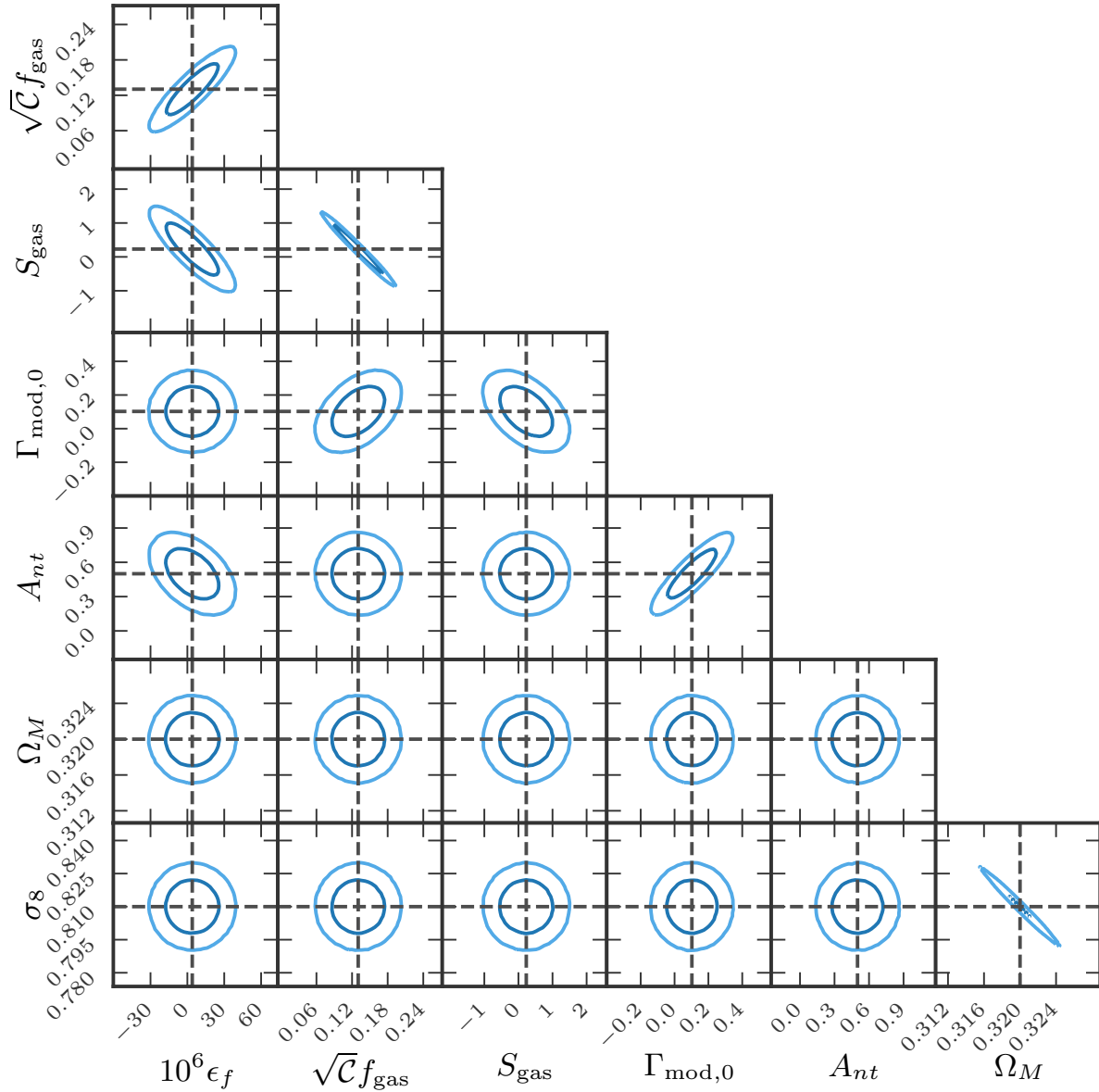


**Figure 4.** Plot showing the Fisher forecasts of the ICM parameters and  $\Omega_M$  and  $\sigma_8$  for the eRASS1 survey. The ellipses denote the 68% and 95% confidence contours of the parameters.

At these multipoles, the model power spectrum matches well with the power spectrum of the *Chandra*/COSMOS field.

- Using Fisher forecast, we predict the upcoming eROSITA All-Sky Surveys (eRASS) will significantly reduce errors on the power spectrum in provide tight constraints on cluster gas mass fraction and cosmological parameters, specifically on  $\Omega_m$  and  $\sigma_8$  at the percent level.

The difference between eFEDS and the *Chandra*/COSMOS field at  $\ell > 2000$  suggests that there is contamination due to resolved point sources that are missed in the eFEDS point source catalog that we used in masking our map. This is in contrast with [Bulbul et al. \(2021\)](#) which found that a significant fraction of extended sources were characterized as point sources. Follow-up observations of the eFEDS sources with *Chandra* will be helpful to understand this potential contamination between extended and point sources.

Alternatively, the differences between eFEDS and the COSMOS field can be due to sample variance, due to the relatively small footprint of COSMOS. Measuring the X-ray angular power spectra for other fields on the sky with existing data will help address the issue of sample variance.

However, even with the restricted multipoles of  $\ell < 2000$  where there are good agreement between observations and model, and where we believe point source contamination is negligible, we can obtain very good constraints on cluster gas fraction,  $\Omega_M$ , and  $\sigma_8$  with the power spectrum of the half-sky eROSITA data. As the X-ray power spectrum measurements is subjected to different systematic uncertainties from other cosmological probes, such as cluster abundance measurements, it can offer complementary and independent constraints on cluster astrophysics and cosmology.



## ACKNOWLEDGEMENTS

We thank Alex Kolodzig for providing his measurements of the power spectrum of extended sources in the *Chandra*/XBootes field. We also thank Kari Helgason for providing the code to estimate clustering power from unresolved point sources. EL and NC were supported by the College of Arts Science of the University of Miami. Á.B., C.J., and W.R.F. acknowledge support from the Smithsonian Institution and the Chandra High Resolution Camera Project through NASA contract NAS8-03060. This work was supported in part by the facilities and staff of the Yale Center for Research Computing. This work is based on data from eROSITA, the soft X-ray instrument aboard SRG, a joint Russian-German science mission supported by the Russian Space Agency (Roskosmos), in the interests of the Russian Academy of Sciences represented by its Space Research Institute (IKI), and the Deutsches Zentrum für Luft- und Raumfahrt (DLR). The SRG spacecraft was built by Lavochkin Association (NPOL) and its sub-contractors, and is operated by NPOL with support from the Max Planck Institute for Extraterrestrial Physics (MPE). The development and construction of the eROSITA X-ray instrument was led by MPE, with contributions from the Dr. Karl Remeis Observatory Bamberg & ECAP (FAU Erlangen-Nuernberg), the University of Hamburg Observatory, the Leibniz Institute for Astrophysics Potsdam (AIP), and the Institute for Astronomy and Astrophysics of the University of Tübingen, with the support of DLR and the Max Planck Society. The Argelander Institute for Astronomy of the University of Bonn and the Ludwig Maximilians Universität Munich also participated in the science preparation for eROSITA. This research made use of data from ROSAT, CXO, eROSITA and several software packages, including astropy (Astropy Collaboration et al. 2013, 2018), CIAO (Fruscione et al. 2006), HEALpix (Górski et al. 2005), and healpy (Zonca et al. 2019).

## DATA AVAILABILITY

The eFEDS data used in this paper are publicly available at <https://erosita.mpe.mpg.de/edr/eROSITA0bservations/Catalogues/>. The ROSAT data used in this paper is available at <http://www.jb.man.ac.uk/research/cosmos/rosat/>. The Chandra/COSMO data and Chandra/XBootes power spectrum data are available upon request. The scripts used to analyze the data are also available upon request.

## REFERENCES

Astropy Collaboration et al., 2013, *A&A*, **558**, A33  
 Astropy Collaboration et al., 2018, *AJ*, **156**, 123  
 Battaglia N., Bond J. R., Pfrommer C., Sievers J. L., 2012, *ApJ*, **758**, 74  
 Benson B. A., et al., 2013, *ApJ*, **763**, 147  
 Bolliet B., Brinckmann T., Chluba J., Lesgourgues J., 2020, *MNRAS*, **497**, 1332  
 Brunner H., et al., 2021, arXiv e-prints, [p. arXiv:2106.14517](https://arxiv.org/abs/2106.14517)  
 Bulbul E., et al., 2021, arXiv e-prints, [p. arXiv:2110.09544](https://arxiv.org/abs/2110.09544)  
 Chadayammuri U., Bogdan A., Oppenheimer B., Kraft R., Forman W., Jones C., 2022, arXiv e-prints, [p. arXiv:2203.01356](https://arxiv.org/abs/2203.01356)  
 Civano F., et al., 2016, *ApJ*, **819**, 62  
 Comparat J., et al., 2020, *The Open Journal of Astrophysics*, **3**, 13  
 Diego J. M., Sliwa W., Silk J., Barcons X., 2003, *MNRAS*, **344**, 951  
 Diemer B., Kravtsov A. V., 2015, *ApJ*, **799**, 108  
 Eckert D., Roncarelli M., Ettori S., Molendi S., Vazza F., Gastaldello F., Rossetti M., 2015, *MNRAS*, **447**, 2198  
 Eckert D., et al., 2019, *A&A*, **621**, A40

Flender S., Nagai D., McDonald M., 2017, *ApJ*, **837**, 124  
 Foster A. R., Ji L., Smith R. K., Brickhouse N. S., 2012, *ApJ*, **756**, 128  
 Fruscione A., et al., 2006, in Silva D. R., Dossy R. E., eds, Society of Photo-Optical Instrumentation Engineers (SPIE) Conference Series Vol. 6270, Society of Photo-Optical Instrumentation Engineers (SPIE) Conference Series. p. 62701V, [doi:10.1117/12.671760](https://doi.org/10.1117/12.671760)  
 Ghirardini V., et al., 2019, *A&A*, **621**, A41  
 Górski K. M., Hivon E., Banday A. J., Wandelt B. D., Hansen F. K., Reinecke M., Bartelmann M., 2005, *ApJ*, **622**, 759  
 Helgason K., Cappelluti N., Hasinger G., Kashlinsky A., Ricotti M., 2014, *ApJ*, **785**, 38  
 Hivon E., Górski K. M., Netterfield C. B., Crill B. P., Prunet S., Hansen F., 2002, *ApJ*, **567**, 2  
 Hurier G., Douspis M., Aghanim N., Pointecouteau E., Diego J. M., Macias-Perez J. F., 2015, *A&A*, **576**, A90  
 Kolodzig A., Gilfanov M., Hütsi G., Sunyaev R., 2017, *MNRAS*, **466**, 3035  
 Kolodzig A., Gilfanov M., Hütsi G., Sunyaev R., 2018, *MNRAS*, **473**, 4653  
 Komatsu E., Seljak U., 2002, *MNRAS*, **336**, 1256  
 Li Y., Cappelluti N., Arendt R. G., Hasinger G., Kashlinsky A., Helgason K., 2018, *ApJ*, **864**, 141  
 Mantz A., Allen S. W., Rapetti D., Ebeling H., 2010, *MNRAS*, **406**, 1759  
 Mantz A. B., et al., 2022, *MNRAS*, **510**, 131  
 Mathiesen B., Evrard A. E., Mohr J. J., 1999, *ApJ*, **520**, L21  
 Mernier F., et al., 2018, *Space Sci. Rev.*, **214**, 129  
 Mirakhor M. S., Walker S. A., 2021, *MNRAS*, **506**, 139  
 Morandi A., Sun M., Mulchaey J., Nagai D., Bonamente M., 2017, *MNRAS*, **469**, 2423  
 Murray S. S., et al., 2005, *ApJS*, **161**, 1  
 Nagai D., Lau E. T., 2011, *ApJ*, **731**, L10  
 Navarro J. F., Frenk C. S., White S. D. M., 1996, *ApJ*, **462**, 563  
 Nelson K., Lau E. T., Nagai D., Rudd D. H., Yu L., 2014, *ApJ*, **782**, 107  
 Osato K., Nagai D., 2022, arXiv e-prints, [p. arXiv:2201.02632](https://arxiv.org/abs/2201.02632)  
 Osato K., Flender S., Nagai D., Shirasaki M., Yoshida N., 2018, *MNRAS*, **475**, 532  
 Osato K., Shirasaki M., Miyatake H., Nagai D., Yoshida N., Oguri M., Takahashi R., 2020, *MNRAS*, **492**, 4780  
 Ostriker J. P., Bode P., Babul A., 2005, *ApJ*, **634**, 964  
 Pillepich A., Reiprich T. H., Porciani C., Borm K., Merloni A., 2018, *MNRAS*, **481**, 613  
 Planck Collaboration et al., 2016, *A&A*, **594**, A22  
 Planck Collaboration et al., 2020, *A&A*, **641**, A6  
 Pratt G. W., Arnaud M., Biviano A., Eckert D., Ettori S., Nagai D., Okabe N., Reiprich T. H., 2019, *Space Sci. Rev.*, **215**, 25  
 Roncarelli M., Ettori S., Borgani S., Dolag K., Fabjan D., Moscardini L., 2013, *MNRAS*, **432**, 3030  
 Salvato M., et al., 2021, arXiv e-prints, [p. arXiv:2106.14520](https://arxiv.org/abs/2106.14520)  
 Shaw L. D., Nagai D., Bhattacharya S., Lau E. T., 2010, *ApJ*, **725**, 1452  
 Shirasaki M., Lau E. T., Nagai D., 2020, *MNRAS*, **491**, 235  
 Snowden S. L., et al., 1997, *ApJ*, **485**, 125  
 Tchernin C., et al., 2016, *A&A*, **595**, A42  
 Tinker J., Kravtsov A. V., Klypin A., Abazajian K., Warren M., Yepes G., Gottlöber S., Holz D. E., 2008, *ApJ*, **688**, 709  
 Tinker J. L., Robertson B. E., Kravtsov A. V., Klypin A., Warren M. S., Yepes G., Gottlöber S., 2010, *ApJ*, **724**, 878  
 Vazza F., Brüggemann M., Gheller C., 2013, *MNRAS*, **428**, 2366  
 Vikhlinin A., et al., 2009, *ApJ*, **692**, 1060  
 Walker S., et al., 2019, *Space Sci. Rev.*, **215**, 7  
 Zandanel F., Weniger C., Ando S., 2015, *J. Cosmology Astropart. Phys.*, **2015**, 060  
 Zhuravleva I., Churazov E., Kravtsov A., Lau E. T., Nagai D., Sunyaev R., 2013, *MNRAS*, **428**, 3274  
 Zonca A., Singer L., Lenz D., Reinecke M., Rosset C., Hivon E., Gorski K., 2019, *Journal of Open Source Software*, **4**, 1298

This paper has been typeset from a  $\text{\LaTeX}$  file prepared by the author.